Key Role of Metal-to-Metal Charge Transfer Transition between Mo^{6+} and Bi^{3+} for Enhancement in NIR Luminescence of Gd_2MoO_6:Bi,Yb Nanophosphor

Taisei Hangai,[1] Takuya Hasegawa,*[,1] Jian Xu,[2] Takayuki Nakanishi,[3] Takashi Takeda,[3] Kosuke Nakano,[4] Kenta Hongo,[4] Ryo Maezono,[4] Tomoyo Goto,[5,6] Yasushi Sato,[7] Ayahisa Okawa,[1] and Shu Yin[1,8]

[1] Institute of Multidisciplinary Research for Advanced Material (IMRAM), Tohoku University, 2-1-1 Katahira, Aoba-ku, Sendai, 980-8577, Japan

[2] International Center for Young Scientists (ICYS), National Institute for Materials Science (NIMS), Tsukuba, Ibaraki 305-0044, Japan

[3] Advanced Phosphor Group, National Institute for Materials Science (NIMS), Tsukuba, Ibaraki, 305-0044, Japan

[4] School of Information Science, Japan Advanced Institute of Science and Technology (JAIST), Asahidai 1-1, Nomi, Ishikawa 923-1292, Japan

[5] SANKEN (The Institute of Scientific and Industrial Research), Osaka University, 8-1 Mihogaoka, Ibaraki, Osaka 567-0047, Japan

[6] Institute for Advanced Co-Creation Studies, Osaka University, 1-1 Yamadaoka, Suita, Osaka, 565-0871, Japan

[7] Department of Chemistry, Faculty of Science, Okayama University of Science, 1-1 Ridai-cho, Kita-ku, Okayama 700-0005, Japan

[8] Advanced Institute for Materials Research (WPI-AIMR), Tohoku University, Sendai 980-8577, Japan

*Corresponding author:
Takuya Hasegawa: hase@tohoku.ac.jp

ABSTRACT

NIR luminescent materials play a significant role in various application fields, including food analysis, medical diagnosis, and bio-imaging. Consequently, there is a growing demand for the development of efficient NIR phosphors. In this study, we successfully synthesized Bi^{3+}-sensitized NIR luminescent nanophosphors, specifically Gd_2MoO_6:Yb, utilizing a solvothermal reaction technique. The luminescent properties were comprehensively assessed with photoluminescence (PL), PL excitation (PLE) spectra, and time-resolved PL spectra at different temperatures. Additionally, electronic structures were estimated to gain insights into the PL mechanism, employing density functional theory (DFT) calculations. It was found that GMO:Bi,Yb exhibited NIR luminescence due to the 4f-4f transitions of Yb^{3+} under ultra-violet light excitation, and the luminescence was sensitized by introducing of Bi^{3+} ions. While the PL spectra in the visible region showed an increased intensity following Bi^{3+} doping, the absence of an additional peak suggested that the enhancement mechanism differs from the typical processes. The time-resolved PL spectra, wavelength-dependent PLE spectra and theoretical calculation of GMO:Bi confirmed that the MMCT transitions between Mo^{6+} and Bi^{3+} ions contributed to its enhancement. The insights from this study should provide valuable concept for developing efficient Yb^{3+}-doped NIR luminescence phosphors.

1. INTRODUCTION

Near-infrared (NIR) light sources have been paid much attention in the fields of food analysis, medical diagnosis, bio-imaging, and agriculture;[1–4] thus, there is a huge demand for NIR luminescence phosphors. Furthermore, it is becoming increasingly important to make the nanoparticles due to its many advantages, for example, high packing density and low light-scattering ability.[5] However, despite their significant importance, NIR nanophosphors have not yet received extensive research Therefore, it is essential to focus on developing efficient ones. In general, inorganic phosphors are comprised of luminescence centers and host materials. As NIR luminescence centers, many researchers chose Eu^{2+} and Ce^{3+} of lanthanide ions or Cr^{3+} and Ni^{2+} of transition metal ions;[6–9] however, their transition types (Eu^{2+}, Ce^{3+}: 4f-5d; and Cr^{3+}, Ni^{2+}: 3d-3d transitions) significantly affect their coordination environment. Consequently, an appropriate host matrix for them should be selected to show the NIR luminescence, which extremely limits the ranges of the host matrix selection. On the other hand, Yb^{3+}, Nd^{3+}, and Er^{3+} of lanthanide ions have an attractive property that they show NIR luminescence regardless of the host matrix due to its 4f-4f intra transitions.[10–12] In particular, Yb^{3+} ions exhibit luminescence around 1000 nm, where matches well with the high responsivity region of silicon. As Yb^{3+} ions possess only one ground state ($^2F_{5/2}$) and one excited state ($^2F_{5/2}$) with an energy difference of approximately 1 eV,[13] the Yb^{3+}-doped NIR phosphors are frequently studied for their applications in solar energy converters for crystalline silicon solar cells and NIR light-emitting diodes.[14,15] In spite of their advantages, the absorption efficiency for the 4f-4f transitions of Yb^{3+} ions is weak and sharp owing to the forbidden transitions.[16] One of the reasonable strategies to improve it is utilizing of energy transfer from ligand to metal charge transfer (LMCT) transitions of the host matrix to Yb^{3+} ions, because LMCT transitions shows efficient and broad absorption due to the allowed transitions.[17,18] Recently, it has been found that LMCT transitions in molybdate between O 2p and Mo 4d orbitals could provide energy to the trivalent lanthanoid ions efficiently.[19] On the other hand, a host matrix containing trivalent lanthanoid ions is appropriate for the doping of Yb^{3+} ions in the host lattice with ease and suppression of the defect generation, because they have similar ionic radius and equivalent oxidation state. Considering what mentioned above, Gd_2MoO_6 (GMO), comprising Gd^{3+} ions of trivalent lanthanoid and molybdate should be suitable as the host matrix for Yb^{3+} ions. In addition, since most molybdates form $[MoO_4]$ units, they have an excitation absorption band in the deep-ultraviolet (DUV) near 300 nm due to a weaker crystal field strength (CFS), *e.g.* $KBaY(MoO_4)_2$:Dy^{3+},Eu^{3+} for λ_{ex}= 317 nm and $K_5Eu_{1-x}Tb_x(MoO_4)_4$ for λ_{ex}= 250 nm.[20,21] On the other hand, the GMO host structure is composed of $[MoO_5]$ trigonal bipyramids, which form stronger CFS, leading that it can be excited by near-UV (NUV) light as reported in Gd_2MoO_6:Eu (λ_{ex}= 355 nm).[22] In terms of practical utilization, the NUV light-excitable phosphors should be more advantageous because of the broader utilization of NUV LEDs.[23] Therefore, GMO should be appropriate host matrix for the Yb^{3+} ions.

In recent years, Bi^{3+} ions have been co-doped as a sensitizer to enhance the luminescence efficiency of lanthanoid ions, for instance, YVO_4:Bi,Ln (Eu^{3+}, Sm^{3+}, and Dy^{3+}) and $LaNbO_4$:Bi,Ln (Eu^{3+}, Tb^{3+}, Dy^{3+}, and Sm^{3+}),[24,25] since the 6s-6p transitions of Bi^{3+} ions supplies another luminescence in addition to the host matrix. Thus, the Bi^{3+} ions are promising luminescence ions for developing outstanding phosphors. It is known that the transitions of Bi^{3+} ions occur between $^1S_0$ ground state of $6s^2$ electronic configuration and triplet $^3P_{0,1,2}$ and singlet $^1P_1$ excited state of $6s^16p^1$ electronic configurations.[26] Following Hund's rules, the energy levels increase from $^3P_0 < {}^3P_1 < {}^3P_2 < {}^1P$,[27] and each transition is denoted A- ($^1S_0 \rightarrow {}^3P_1$), B- ($^1S_0 \rightarrow {}^3P_2$) and C-transitions ($^1S_0 \rightarrow {}^1P_1$), respectively. Especially, A-transitions are commonly observed in UV or NUV region,[28] and the energy should be expected to match the excitation bands of lanthanoid-doped GMO.[29] Therefore, doping of Bi^{3+} ions in GMO:Yb should contribute to the enhancement of NIR luminescence in GMO:Yb. However, Bi^{3+} ions doped in host matrix containing d^0 cation (M^{n+}: Ga^{3+}, Mo^{6+}, Ti^{4+}, V^{5+}, Nb^{5+}, and W^{6+} *etc.*) also shows the metal-to-metal charge transfer (MMCT) transitions ($Bi^{3+}(6s^2) + M^{n+}(d^0) \rightarrow Bi^{4+}(6s^1) + M^{(n-1)+}(d^1)$) besides the $6s^2 \rightarrow 6s^16p^1$ interconfigurational transitions,[30–33] which makes the luminescence mechanism extremely complicate. Particularly, ascribing the luminescence in Bi^{3+}-doped molybdate phosphor is quite difficult reported in Bi^{3+}-doped lanthanum molybdate (La_2MoO_6:Bi and

$La_2Mo_2O_9$:Bi);[34] thus, it should be challenging studies to uncover the luminescence mechanism of Bi^{3+}-doped molybdate phosphor. On the other hand, understanding it could provide us with great progress in developing an effective material design concept using Bi^{3+} ions as a sensitizer for Yb^{3+} ions. In this research, we focused on the synthesis and evaluation of the luminescence property of novel NIR nanophosphor GMMO:Bi,Yb. Furthermore, its luminescence mechanism was successfully uncovered by combining experimental and theoretical analyses. These perspectives could be useful in developing an efficient NIR luminescence phosphor.

2. Methods

2.1 Materials. Raw chemicals for synthesis of GMO:Bi,Yb phosphor materials of $Gd(NO_3)_3\cdot 6H_2O$ (>99.95%) and $(NH_4)_6Mo_7O_{24}\cdot 4H_2O$ (>99.0%) were purchased from Kanto Chemical Co., Inc., Japan and that of $Bi(NO_3)_3\cdot 5H_2O$ (>99.5 %), $Yb(NO_3)_3\cdot nH_2O$ (>99.9%) and isopropanol (>99.7%) were purchased from Fujifilm Wako Pure Chem.Co., Japan, respectively. The hydration amount in $Yb(NO_3)_3\cdot nH_2O$ was estimated by thermogravimetry, which was found to be 5.9 for n.

2.2 Synthesis of GMO:Bi,Yb nanophosphors. The GMO:Bi,Yb nanophosphors were synthesized by a solvothermal reaction method in an alcohol solvent. In a typical synthesis, metal nitrates (total 2 mmol) of $Gd(NO_3)_3\cdot 6H_2O$, $Bi(NO_3)_3\cdot 5H_2O$, $Yb(NO_3)_3\cdot nH_2O$, and $(NH_4)_6Mo_7O_{24}\cdot 4H_2O$ (1 mmol) were added to 40 ml of isopropanol under a vigorous stirring condition for *ca.* 10 min. Subsequently, this colloidal solution was transferred to a 100 ml Teflon-lined autoclave vessel and heated at 220 ºC for 5 h in an oven. After cooling to room temperature, the precursor was washed with water and ethanol, was collected by filtration, and then dried at 60 ˚C for 1 h under ambient pressure. Finally, the pale-gray-colored precursor powder was annealed at 850 °C for 5 h using an electric furnace to obtain a series of GMO nanophosphors.

2.3 Characterization. The chemical composition was analyzed with X-ray photoelectron spectroscopy (XPS, PHI5600, ULVAC-PHI Inc.). The crystal phase was determined by powder X-ray diffraction (XRD) using X-ray diffractometer (D2 PHASER, Bruker) with CuKα radiation ($\lambda = 1.5406$ nm). The detailed structural information was refined by Rietveld analysis technique using a RIETAN-

FP program package.[35] To obtain the chemical states of each metal component, the X-ray absorption fine structure (XAFS) analysis for the Gd, Yb and Bi L_3-edges and Mo K-edge was utilized by BL12C (Gd, Bi and Yb L_3-edges) and NW10A (Mo K-edge) beamlines in the Photon Factory (PF) at High Energy Accelerator Research Organization, Japan (KEK). The sample was diluted by boron nitride powder and pelleted for the measurement. The measurement mode of Gd and Yb L_3-edge and Mo K-edge was transmission mode and one of Bi L_3-edge was fluorescence mode since the amount of Bi was low. The obtained data from XAFS was analyzed by Athena and Artemis programs.[36] The diffuse reflectance spectra (DRS) were measured by UV-vis-NIR spectrometer (V-670, JASCO Corp.) conducted with an integrated sphere attachment. The morphology was observed by transmission electron microscope (TEM, EM-002B (Topcon Corp.)). The thermal stability was measured by a Thermogravimeter-Differential Thermal Analyzer (TG-DTA8122, Rigaku). The photoluminescence (PL) and PL excitation (PLE) spectra and quantum efficiencies were measured by spectrofluorometer (FP-8700, JASCO Corp.) equipped with a 150 W Xe lamp as an excitation source. The temperature-dependent PL and PLE spectra and PL lifetimes of NIR luminescence due to Yb^{3+} ions were recorded by photoluminescence spectrometer (FLS1000-SD-stm, Edinburgh Inst.) equipped with 450 W Xe lamp and the measurement temperature was controlled by thermal stage (THMS600, Linkam Scientific Instruments). The time-resolved luminescence spectroscopy was measured by an optical setup mainly composed of Ti:Sapphire solid-state laser with an optical parametric generator (OPG; Chameleon Vision-S, Coherent, inc.), 3D Raman confocal microscope system, high-resolution monochromator, and streak camera. The powder sample was dispersed by the ethanol on a copper substrate. The sample was excited with OPG pumped by a pulsed Ti:Sapphire laser with emission wavelength 710 nm, which could generate the second harmonic generation (SHG) laser beam at 355 nm with 75 fs pulse width and 100 μs repetition rate. The 3D Raman confocal microscope system (Nanofiber 30, Tokyo Instrument Inc.) act as a real-time imaging spectrometer to monitor the emission of the sample under the optical parametric oscillator laser excitation. The reflected optical signal through a fluorescence microscope (BX51M, Olympus Co., Ltd) was collected high-resolution monochromator (SpectraPro

HRS-300, Princeton Instruments) and a streak camera (C14831-110, Hamamatsu Photonics Co., Ltd.). The emission spectral range was monitored between 485 nm and 810 nm with a 40 g min^{-1} grating grove. The timescale for the measurement was set to 50 μs, and temperature-dependent experiments were performed in a microscopy cryostat (Janis ST-500, Lake Shore Cryotronics) with the temperature control set at 6 K.

2.4 Theoretical calculation. Our first-principles calculations were conducted with Quantum Espresso package.[37] The ionic core and core electrons were replaced with PAW (Projected Augmented Wave) pseudopotentials in the SSSP Precision library,[38] and hence the valence electrons were $2s^22p^4$ for O, $4d^45s^2$ for Mo, $4f^85d^06s^26p^0$ for Gd, $4f^{14}5d^{10}6s^26p^3$ for Bi. The exchange-correlation effects were described by the Perdew-Burke-Ernzerhof revised form for solids (PBEsol) of generalized gradient approximation (GGA),[38] together with the Hubbard corrections with $U = 4$ eV for Mo atoms, 6 eV for Gd atoms and 4 eV for Yb atoms.[39–41] Crystal structure models in simulation cells were made by considering the structure of Gd_2MoO_6 and Gd_2MoO_6:Bi as $Gd_8Mo_4O_{24}$ and $Gd_7BiMo_4O_{24}$, respectively. Furthermore, the crystal structure was transformed into the primitive cell to reduce the calculation costs. A plane-wave cutoff energy of 90 Ry, a k-point sampling of 3×4×7 grid, and an energy convergence of 1.0×10^{-4} eV/atom were used for all the calculations. After the structure optimization, densities of states (DOS) and projected density of state (pDOS) were calculated.

3. RESULTS AND DISCUSSION

The chemical compositions of GMO, GMO:Bi (1 mol% Bi^{3+}), GMO:Yb (8 mol% Yb^{3+}), and GMO:Bi,Yb (1 mol% Bi^{3+}, 8 mol% Yb^{3+}) were firstly analyzed by XPS measurement. From the wide scan survey (Figure 1(a)), all sample exhibits the peaks derived from the Gd and Mo elements, whereas additional peaks attributed to the Bi and Yb elements appeared in Bi or Yb doped samples (Figure 1(b)). For the quantitative analysis for estimating the molar ratio of Gd/Bi/Yb in all GMO nanophosphors, the signals of Gd, Bi, and Yb were integrated, which was summarized in Table S1. In addition, the oxidation state determinations of each element were carried out from the narrow scan analysis (Figure S1 and Figure 1(b)). The Gd 4d spectra (Figure S1 (a)) showed that the two peaks at 141 and 147 eV were ascribed to the Gd $4d_{5/2}$ and $4d_{3/2}$, respectively, suggesting that Gd ions take trivalent.[42] In the Mo 3d spectra (Figure S1 (b)), the peaks of Mo $3d_{5/2}$ and $3d_{3/2}$ were centered at 232 and 235 eV, respectively, indicating that the Mo atoms exist in Mo^{6+} ions. [43] The two peaks at 164 and 159 eV were assigned to Bi $4f_{5/2}$ and $4f_{7/2}$, respectively, meaning the Bi^{3+} state,[44] and the Yb 4d spectra showed one peak at 184 eV, implying the existence of Yb^{3+} ions (Figure 1(b)).[45] Because it is known that XPS is the surface-sensitive measurement,[46] the oxidation states of the bulk were also evaluated by comparing the absorption edge position for Gd L_3-, Bi L_3-, Yb L_3- and Mo *K*-edges using X-ray absorption near edge structure (XANES) spectra as shown in Figure S2. The positions for all samples were consistent with Gd_2O_3, Bi_2O_3, and Yb_2O_3, as a reference, indicating that their oxidation states took trivalent similar to the XPS results, while ones of Mo *K*-edge corresponded with MoO_3 with hexavalent molybdenum. It was concluded that the oxidation state of Gd, Bi, and Yb was trivalent, and Bi^{3+} and Yb^{3+} ions should be substituted into Gd^{3+} site in terms of oxidation state. Figure 1(c) shows TEM images of each GMO nanophosphors. All GMO nanophosphors have the sphere-like morphology with the size of 50-100 nm. The nano-sized particles are precisely due to the solvothermal reaction. Furthermore, the dramatical changes in the morphology by doping were not observed; thus, even samples synthesized with different chemical compositions are suitable for comparative evaluation of structural and optical properties. The Thermogravimeter-Differential Thermal Analyzer (TG-DTA) analysis from 330 K to 1000 K under ambient air (Figure S3) indicated that GMO:Bi,Yb nanophosphor was stable under high temperature since there was no obvious weight loss and endothermic and exothermic peaks.

The crystal structure of all GMO nanophosphors was determined by the powder X-ray diffraction (XRD) method. Figure 2(a) shows the results of the Rietveld refinement profiles of all GMO nanophosphors. The observed peaks were fitted well with simulated patterns of monoclinic Gd_2MoO_6 structure with space groups of $C2/c$ (No. 15), and it was found to be low values for the *R*-factors (R_{wp} < 11 %), meaning that it is succeeded the reliable refinements. The refined lattice parameters for all

GMO nanophosphors were summarized in Table S2, and the cell volumes (*V*) were estimated to be 950(1) Å^3 for GMO:Bi, 949(1) Å^3 for GMO, 942.7(4) Å^3 for GMO:Bi,Yb, and 941.2(8) Å^3 for GMO:Yb (Figure 2(b)). The minor difference indicates that Bi^{3+} and Yb^{3+} ions were successfully substituted into Gd^{3+} ions since there was a correlation between ionic radius under an 8-corrdination environment (1.17 Å for Bi^{3+}, 1.05 Å for Gd^{3+}, and 0.985 Å for Yb^{3+})[47] and the unit cell of each GMO nanophosphors. The crystal structure of the GMO host can be illustrated as Figure 2(c) using the VESTA program.[48] There are three crystallographically different Gd sites (Gd1,2,3) with 8-fold coordination and one Mo site with 5-fold coordination in Gd_2MoO_6, and the structure was composed of alternating layers of Gd layers (Gd1 and Gd2) and Gd-Mo layers (Gd3 and Mo).[49] In addition, the Gd1 and Gd2 occupy the C_2 point site, on the other hand, Gd3 occupies C_1 point site. It is known that the coordination environment of the doping site strongly affects the luminescence property; thus, it was estimated by the comparisons of the total energy after structural optimization calculated with DFT calculations. Table S3 summarizes the lattice parameter and average bond length between cation and oxygen obtained from CIF (ICSD #162866), DFT calculation, and Rietveld analysis. It was found that the differences in lattice parameter and bond length were less than 1 %, indicating that the DFT-optimized geometry was reliable. The stability after doping of Bi^{3+} and Yb^{3+} ions was evaluated with eq (1):

$$\Delta E = E_{\mathrm{host}} - E_{\mathrm{Gd}(n)} \tag{1}$$

where E_{host} and $E_{\mathrm{Gd(n)}}$ were the total energy of the $Gd_8Mo_4O_{24}$ and $Gd_7XMo_4O_{24}$ (X= Bi and Yb in each Gd site). The ΔE values for each Gd site were found to be almost the same values (Figure S4 and Table S3), which means that Bi^{3+} and Yb^{3+} ions should be substituted uniformly in all Gd sites due to the relatively similar environment in three Gd sites. Furthermore, comparing the average bond length between the Gd and O atoms (Gd1-O: 2.4488 Å, Gd2-O: 2.4227 Å, Gd3-O: 2.4053 Å) with the ΔE values, it was not found to be the relationship between each Gd site. The ΔE values for Yb^{3+} were smaller than the ones for Bi^{3+}, which means that the substitution of Yb^{3+} ions should be energetically more favorable than Bi^{3+} ions.

Figure 3(a) shows the diffuse reflectance spectra (DRS) of the GMO nanophosphors. All GMO nanophosphors had broad absorption from 200 nm to 400 nm attributed to the LMCT transitions between O 2p orbital and Mo 4d orbital in the [MoO_5] unit. The LMCT transitions between O 2p orbital and Yb 5d orbital was not observed in the Yb^{3+}-doped sample, because the increase of reflectance was not observed in that region as related tungstate materials, *e.g.* Lu_2WO_6:Yb.[13] Meanwhile, the absorption due to the $^2F_{7/2} \rightarrow {}^2F_{5/2}$ transitions in Yb^{3+} ions were observed in NIR region around 1000 nm, and the Bi-doped samples showed an absorption around 500 nm. The optical band gap for each sample was estimated by Tauc-plot and Kubelka-Munk transformation expressed with eq (2) and (3):[22]

$$(h\nu\alpha)^{\frac{1}{2}} = A(h\nu - E_g) \qquad (2)$$

$$\alpha = \frac{(1-R)^2}{2R} \qquad (3)$$

where $h\nu$, α, A, E_g, and R represent the photon energy, absorption coefficient, absorption constant, band gap energy, and reflectance coefficient, respectively. The E_g values of GMO, GMO:Bi, GMO:Yb, and GMO:Bi,Yb were estimated to be 2.90, 2.74, 3.01, and 2.96 eV, respectively (Figure 3(b)). The value of GMO was almost consistent with the reported energy of 2.7 eV.[22] For the discussion of different E_g values in each GMO nanophosphor, it is important to consider the conduction band minimum (CBM) formed by Mo 4d orbitals since they were strongly influenced by the crystal field, namely the distance between Mo and O atoms. It is known that accompanied by the shortening of the bond length between the transition metal ion and anion, the crystal field becomes stronger, resulting that the position of CBM formed by the transition metal shifted to a lower energy side. Thus, the bond length between Mo and O atoms was estimated with EXAFS analysis as shown in Figure S5. The main peaks were observed at around 1.4 Å in a radial distance, where originating from the first coordination sphere of Mo atoms surrounded by O atoms, and the bond lengths were 1.78 Å for GMO and GMO:Bi nanophosphors and 1.79 Å for GMO:Yb and GMO:Bi,Yb nanophosphors. It exhibited a shift towards a longer radial distance by Yb^{3+} doping. It indicated that the effect in GMO and GMO:Bi is stronger than one in GMO:Yb and GMO:Bi,Yb, resulting in the shift of CBM towards higher energy side by Yb^{3+} doping, which was consistent with the increase of E_g values. In contrast, the E_g values decreased by Bi^{3+} doping, and it might be due to the formation of the hybrid orbital formed by O 2p and Bi 6s orbitals. For further understanding of the effect of Bi^{3+} ions on their optical properties, the DOS/pDOS of the GMO and GMO:Bi (substituted in the Gd1 site) were calculated as shown in Figure 4. Since the obtained band gap energy of GMO (1.8 eV) was consistent with the previous report (1.9 eV),[50] the accuracy of this calculation was ensured. In both materials, the bottom of the conduction bands was formed by Mo 4d orbitals. Although, in the valence band maximum (VBM), they were composed by only O 2p orbitals for GMO, they formed the hybridization orbitals between O 2p and Bi 6s orbitals for GMO:Bi. It means that the absorption in the UV region for the Bi^{3+}-doped sample was attributed to the LMCT (O 2p/Mo 4d) and MMCT (Bi 6s/Mo 4d) transition due to the formation of Bi 6s/O 2p hybrid orbitals in Figure 3. Moreover, the hybrid orbitals caused the upper shift of the VBM, resulting in a decrease of the band gap energy from 1.8 to 1.5 eV. The difference was consistent with the experimental results, such as the decrease of the band gap for UV-vis spectra. It was found that Bi 6s orbitals directly affect the VBM in GMO, and moreover, Bi^{3+} ions should be doped into all Gd site, thus the substituted site-dependent DOS/pDOS calculations were performed (Figure S6). Herein, only Gd1 and Gd3 site were focused for the comparison, since it was considered that the Gd1 and Gd2 sites lie in similar environment forming Gd layer in the lattice as visualized in Figure 2(c). In the case of Bi^{3+} substituted in Gd3 site, although the band gap narrowing was not observed, the DOS in VBM (Figure S6(b)) increased compared with matrix, meaning the promotion of the electronic transitions from VB to CB, which was consistent with the additional absorption in 500 nm by Bi^{3+} doping in DRS spectra and Kubelka-Munk spectra (Figure 3(a) and Figure S7). Thus, it was confirmed that Bi^{3+} ions were substituted in all three Gd sites from the relation between absorption property and DOS/pDOS.

Photoluminescence (PL) and PL excitation (PLE) spectra of Yb^{3+}-doped GMO nanophosphors in the NIR region at room temperature are shown in Figure 5(a). The PLE spectra of GMO:Yb and GMO:Bi,Yb nanophosphors monitored at 975 nm have a broad excitation band ranging from 300 to

500 nm with a peak at 363 nm due to the LMCT transitions between O 2p and Mo 4d orbitals. Additionally, the normalized PLE spectra (inset of Figure 5(a)) showed a slight redshift of the peak position from 360 to 363 nm by Bi^{3+} co-doping, which was consistent with the decrease of band gap energy in UV-vis spectra and theoretical calculation. The PL spectra excited at 363 nm shows NIR emission ranging from 900 to 1100 nm corresponding to $^2F_{5/2} \rightarrow {}^2F_{7/2}$ transitions of Yb^{3+} ions with the strongest peak at 975 nm. It contained splitting five sharp peaks at 950, 975, 1040, 1050, and 1170 nm, which derived from the crystal field splitting of $^2F_{5/2}$ and $^2F_{7/2}$ levels.[13] The internal PL quantum yields of GMO:Yb and GMO:Bi,Yb in the NIR region under 363 nm excitation were found to be 2.45 and 3.24 %, respectively. The remarkable increase in PL intensity indicates that the Bi^{3+} ions work as a sensitizer for the luminescence of Yb^{3+} ions. From the decay curve of GMO:Yb and GMO:Bi,Yb at room temperature (λ_{ex}= 360 nm, λ_{em}= 975 nm) as shown in Figure S8, the curves followed with double exponential expressed by eq (4):

$$I(t) = A_1 \exp\left(-\frac{t}{\tau_1}\right) + A_2 \exp\left(-\frac{t}{\tau_2}\right) \tag{4}$$

where the $\tau_{1,2}$, $A_{1,2}$, and $I(t)$ represent decay times, fitting components, and the intensities at time t, respectively. The presence of two decay components suggests the existence of two decay process. Therefore, it is estimated that Yb ions were doped in two Gd site at least, which matches with the theoretical estimation of doping site. The fitting values are summarized in Table S5, and the average lifetime (τ_{ave}) were calculated following equation:

$$\tau_{\text{ave}} = \frac{A_1\tau_1^2 + A_2\tau_2^2}{A_1\tau_1 + A_2\tau_2} \tag{5}$$

The average lifetimes of GMO:Yb and GMO:Bi,Yb were found to be 203, and 207 μs, respectively. They took similar values with reported ones of Yb^{3+}-doped transition-metal oxide phosphors, for instance, 189 μs for $NaGd(WO_4)_2:Yb^{3+}$ and 340 μs for $CaNb_2O_6:Yb$.[51,52] Figure S9 shows the PL spectra and decay curves of GMO:Bi with varying concentrations of Yb^{3+} ions (5, 7, 8, 9, and 10 mol%). The intensity increased with increasing of Yb^{3+} ions up to 8 mol% and then decreased beyond 8 mol% due to the concentration quenching of Yb^{3+} ions, while the lifetime (Table S6) decreased as the amount of Yb^{3+} ions increased, meaning that interaction between Yb^{3+} ions became intense.[53] Then, the PL and PLE spectra of GMO and GMO:Bi in the visible region at 77 K were measured (Figure 5(b)) to understand the contribution of the enhancing emission by Bi^{3+} ions doping. The PLE spectra of GMO and GMO:Bi nanophosphors monitored at 670 nm showed a broad excitation band ranging from 300 to 500 nm. The peak position shifted from 350 nm to 362 nm by Bi^{3+} doping, which was consistent with the PLE spectra in the NIR region. The PLE spectra were fitted well with one and two Gaussian functions for GMO and GMO:Bi, respectively as shown in Figure S10. The transition in PLE spectra for GMO was attributed to the LMCT transition between O 2p and Mo 4d orbitals. On the other hand, the PLE spectra for GMO:Bi contained two transitions, suggesting that additional transition should be due to the Bi^{3+} doping. The PL spectra excited at 350 and 362 nm have a broad band from 500 to 800 nm centered around 670 nm. It was observed that the intensity was enhanced by Bi^{3+} ions as well as in the NIR region. However, no significant difference was observed between pristine and Bi^{3+}-doped samples except for the increase in luminescence intensity, such as the additional luminescence bands due to the Bi^{3+} ions as observed in other Bi^{3+}-activated phosphors such as Ca_2MgWO_6:Bi^{3+} and $LuVO_4$:Bi^{3+}.[32,54] In some cases, the luminescence property depends on the Bi^{3+} doping amount,[55] thus the concentration-dependent PL spectra of GMO:xBi (x = 0.5, 1, 2, and 3 mol%) were measured (Figure S11). The PL intensity became the maximum in x= 1 mol%, and it was found for the appropriate amount of Bi^{3+} ions to be 1 mol %. The change with the different Bi^{3+} concentrations was a typical concentration quenching process. To confirm the energy transfer process, the PL spectra of GMO:Bi,yYb (y = 0, 0.5 and 1 mol%) in visible and NIR region were measured at 77 K as shown in Figure 5(c). The PL intensity in the visible region gradually decreased with the increase of Yb^{3+} contents, whereas one in the NIR region increased, which means that it was a typical energy transfer process shown in many phosphors. In addition, the lifetime of GMO:Bi,yYb in the visible region at 77K was measured (Figure 5(d)), and the lifetime summarized in Table S7 shortened along with the increase of Yb^{3+} ions. The energy transfer efficiencies (η_{ETE}) were estimated by the following equation eq (6):

$$\eta_{\mathrm{ETE}}\ (\%) = (1 - \frac{\tau_x}{\tau_0}) \times 100 \tag{6}$$

where τ_x and τ_0 represent the average lifetime at 670 nm with and without Yb^{3+} ions. The values were found to be 21 % for 0.5 mol% and 51 % for 1 mol%. The η_{ETE} values increased with increasing Yb^{3+} concentration, which suggested that the energy transfer occurs from the matrix to Yb^{3+} ions.

To reveal the enhancing mechanism in PL intensity, temperature-dependent luminescence property in visible and NIR region of GMO, GMO:Bi, GMO:Yb, and GMO:Bi,Yb was evaluated (Figure 6). From the temperature-dependent PL spectra for all GMO nanophosphors (Figure 6(a) and (b)), there were no shape changes of the spectra or the peak shifts at each temperature, and it was only observed to decrease the intensity gradually with increasing temperature. In addition, from 77 K to 300 K, it was not observed the difference in the quenching behavior between Bi^{3+}- and non-doped samples in both the visible and NIR regions. Therefore, it should not critically contribute to the enhancement of the luminescence intensity by Bi^{3+} doping.

A more in-depth evaluation of each GMO nanophosphor was essential for the further evaluation of the enhancing mechanism. Hence, time-resolved spectroscopy, a powerful tool for clarifying complex luminescence properties, was performed at 6 K. Figure 7(a) shows the streak image at 6 K, time-dependent PL spectra, and wavelength-dependent decay curves of GMO:Bi excited at 355 nm. The difference between the spectra obtained from the streak image and Figure 5(b) was due to the uncorrected responsivity of its spectrometer. However, the difference should not be a problems in this case, because it was measured for understanding the luminescence mechanism of GMO:Bi. The wavelength-dependent decay curves were successfully fitted by eq (4), and the fitting parameters were summarized in Table 1. It was found that the lifetime (τ_1 and τ_2) from 480 to 550 nm was clearly shorter than that beyond 550 nm. To assign their luminescence components, a series of varied wavelength-dependent PLE spectra (λ_{em} = 670, 570 and 530 nm) for GMO:Bi were measured at 77 K (Figure 7(b)). The PLE spectrum monitored at 670 nm was deconvoluted two components, namely PLE(1) in the lower energy side, and PLE(2) in the higher energy side. The intensity ratio of PLE(2) to PLE(1) ($I_{\mathrm{PLE(2)}}/I_{\mathrm{PLE(1)}}$) was found to be 1.6 at λ_{em} = 670 nm. On the other hand, in the PLE spectrum at 570 nm, the ratio of $I_{\mathrm{PLE(2)}}/I_{\mathrm{PLE(1)}}$ was found to be 2.7, which suggested that the contribution of PLE(2) increases by shifting the monitored wavelength, and the PLE spectra monitored at 530 nm was composed with only PLE(2) peaking at 346 nm. Therefore, from the wavelength-dependent PLE spectra, it can be inferred that the excitation energy of the emission band from 480 to 550 nm was larger than that of the band after 550 nm. To clarify the emission components of PLE(1) and PLE(2), the excitation energy of the MMCT (Bi 6s → Mo 4d) and A-transitions ($^1S_0 \rightarrow {}^3P_1$) of the Bi^{3+} was evaluated with the theoretical method. Focusing on the position of the Bi 6p orbitals in the DOS/pDOS of GMO:Bi (Figure S12), the orbitals lay on 0.2 eV higher energy side than the bottom of the conduction band formed by Mo 4d orbitals. In addition to the DFT calculation, the MMCT and A-transitions energy were also estimated using the empirical equation. The MMCT energy in coordination numbers larger than 4 of Mo atoms can be predicted following equation:[56]

$$\mathrm{MMCT}\ (\mathrm{Bi}^{3+}, \mathrm{cm}^{-1}) = 54{,}999 - 45{,}556\frac{\chi_{\mathrm{CN}'}(\mathrm{Mo}^{6+})}{d_{\mathrm{corr}}} \tag{7}$$

where $\chi_{\mathrm{CN}'}(\mathrm{Mo}^{6+})$ represents the optical electronegativity of the Mo^{6+} ions[57] and d_{corr} is the corrected distance between Bi^{3+} and Gd^{3+} ions. The d_{host}, the shortest distance between Mo site and Bi site[58], can be calculated from

$$d_{\mathrm{corr}} = d_{\mathrm{host}} + \frac{1}{2}[r(\mathrm{Bi}^{3+}) - r(\mathrm{host})] \tag{8}$$

where $r(\mathrm{Bi}^{3+})$ and $r(\mathrm{host})$ represent the ionic radius of the Bi^{3+} ions and the ionic radius of the host cation substituted by Bi^{3+} ion (Gd^{3+} in this case), respectively. On the other hand, the energy of the A-transitions can be estimated by the following empirical equation.[59]

$$E_A(\mathrm{cm}^{-1}) = 23790 + 50051e^{-h_e/0.551} \tag{9}$$

where h_e is the environmental factor containing covalence, coordination number, bond volume polarizability and presented charge.[60] From the calculated values summarized in Table 2, it was found that the MMCT energy (Gd1: 3.15 eV, Gd2: 3.37 eV, Gd3: 3.25 eV) was smaller than A-transitions energy (Gd1: 3.33 eV, Gd2: 3.44 eV, Gd3: 3.30 eV). Since the empirical equations could not estimate the energy completely, the estimated values were not consistent with the observed one (PLE(1): 3.3 eV (371 nm), PLE(2): 3.5 eV (351 nm)). However, these results were valid because the order of energy magnitude was consistent with the DFT calculation. Therefore, the PLE(2) (higher energy) and PLE(1) (lower energy) were assigned to A-transitions of Bi^{3+} ions and MMCT transitions, respectively It was concluded that the MMCT transition between Bi 6s and Mo 4d contributed to the enhancement of the luminescence in the visible region, resulting in the enhancement in the NIR region. Herein, PLE(1) should contain the LMCT and MMCT transitions since the energy difference between them was extremely small not to deconvolute into two excitation bands. On the other hand, in the PL spectra for GMO:Bi nanophosphors at 77 K, the reason for the absence of the emissions related to the Bi^{3+} ions should be that the energy transfer from Bi^{3+} to MMCT excited state occurred in GMO:Bi nanophosphors.

4. Conclusion

In this work, new NIR luminescence nanophosphor Gd_2MoO_6:Bi,Yb (GMO:Bi,Yb) was synthesized via a solvothermal reaction method, and its luminescence property was deeply evaluated. Based on the structural analysis, it was confirmed that Bi^{3+} and Yb^{3+} ions were successfully doped into Gd^{3+} site. The GMO:Bi,Yb nanophosphors exhibited NIR luminescence around 975 nm under 363 nm excitation by the energy transfer, and Bi^{3+} ions worked as a sensitizer for the luminescence of Yb^{3+} ions, since the PL intensity was enhanced by Bi^{3+} co-doping. From the PL spectra in visible region of GMO and GMO:Bi, the intensity also increased by Bi^{3+} doping; however, the sensitization mechanism of Yb^{3+} ions was not uncleared. On the other hand, the wavelength-dependent decay curves obtained from time-resolved spectroscopy at 6 K indicated that the lifetime from 480 to 550 nm was obviously shorter than one beyond 550 nm. From the tendency of the varied-wavelength PLE spectra (λ_{em} = 670, 570, and 530 nm), the excitation energy of the emission band from 480 to 550 nm was higher than one after 550 nm. Furthermore, the DOS/pDOS and empirical calculation revealed that the emissions in before and after 550 nm were assigned to the $^3P_1 \rightarrow {}^1S_0$ transitions of Bi^{3+} ions and the MMCT transitions between Bi^{3+} and Mo^{6+} ions, respectively. Therefore, the MMCT transitions between Bi^{3+}

and Mo^{6+} ions contributed to the enhancement of the visible and NIR luminescence. These findings should help design a new Yb^{3+}-doped NIR luminescence phosphor with Bi^{3+} sensitization.

Supporting Information

The Supporting Information is available free of charge at xxx.

XPS spectra, XANES spectra, ΔE values, EXAFS, DOS/pDOS, Kubelka-Munk spectra, decay curve, PL spectra, crystallographic parameters, and fitting parameter of the decay curve in NIR and visible region.

Acknowledgements

This work was supported by research granted from The Murata Science Foundation, JSPS KAKENHI Grant Numbers (20K15106, 22K05264, and 20H00297), Feasibility Study for Young Researchers (FS) in "Crossover Alliance to Create the Future with People, Intelligence and Materials", JST, the establishment of university fellowships towards the creation of science technology innovation, Grant Number JPMJFS2102, and NIMS Joint Research Hub Program. The XAFS measurements were performed with the beamlines of BL12C and NW10A at the PF with the approval of the High Energy Accelerator Research Organization (KEK) (2020P001 and 2021G608). The XPS measurements were performed with the TAGEN-CAF. The computations in this work have been performed using the facilities of Research Center for Advanced Computing Infrastructure at JAIST. R.M. is grateful for financial supports from MEXT-KAKENHI (JP22H05146, JP21K03400 and JP19H04692), from the Air Force Office of Scientific Research (AFOSR-AOARD/FA2386-17-1-4049;FA2386-19-1-4015).

References

(1) Zhao, F.; Cai, H.; Song, Z.; Liu, Q. Structural Confinement toward Controlling Energy Transfer Path for Enhancing Near-Infrared Luminescence. *Chem. Mater.* **2021**, *33* (21), 8360–8366.

(2) Goswami, S.; Das, A. K.; Maity, A. K.; Manna, A.; Aich, K.; Maity, S.; Saha, P.; Mandal, T. K. Visual and near IR (NIR) Fluorescence Detection of Cr^{3+} in Aqueous Media via Spirobenzopyran Ring Opening with Application in Logic Gate and Bio-Imaging. *Dalton Trans.* **2013**, *43* (1), 231–239.

(3) Tan, T.; Wang, S.; Su, J.; Yuan, W.; Wu, H.; Pang, R.; Wang, J.; Li, C.; Zhang, H. Design of a Novel Near-Infrared Luminescence Material $Li_2Mg_3TiO_6:Cr^{3+}$ with an Ultrawide Tuning Range Applied to Near-Infrared Light-Emitting Diodes. *ACS Sustainable Chem. Eng.* **2022**, *10* (12), 3839–3850.

(4) Liu, G.; Molokeev, M. S.; Xia, Z. Structural Rigidity Control toward Cr^{3+}-Based Broadband Near-Infrared Luminescence with Enhanced Thermal Stability. *Chem. Mater.* **2022**, *34* (3), 1376–1384.

(5) Terraschke, H.; Wickleder, C. UV, Blue, Green, Yellow, Red, and Small: Newest Developments on Eu^{2+}-Doped Nanophosphors. *Chem. Rev.* **2015**, *115* (20), 11352–11378.

(6) Tang, Z.; Du, F.; Zhao, L.; Liu, H.; Leng, Z.; Xie, H.; Zhang, G.; Wang, Y.; Tang, Z.; Du, F.; et al. Single-Site Occupancy of Eu^{2+} in Multiple Cations Enables Efficient Ultra-Broadband Visible to Near-Infrared Luminescence. *Laser Photonics Rev.* **2023**, *17* (5), 2200911.

(7) Zhu, Y.; Wang, X.; Qiao, J.; Molokeev, M. S.; Swart, H. C.; Ning, L.; Xia, Z. Regulating Eu^{2+} Multisite Occupation through Structural Disorder toward Broadband Near-Infrared Emission. *Chem. Mater.* **2023**, *35* (3), 1432–1439.

(8) Lingxiang Chu; Yi Qin; Tao Yang; Jing Wan; Qiang Zhou; Huaijun Tang; Yanqing Ye; Zhengliang Wang. Near-Infrared Luminescence and High Thermal Stability of $Rb_2NaScF_6:Cr^{3+}$ Phosphor for Spectroscopy Applications. *Adv. Mater.* **2023**, *4* (19), 4583-4589.

(9) Zhu, F.; Gao, Y.; Ding, J.; Qiu, J. Synergistic Enhancement of the Near-Infrared Luminescence Properties of Ni^{2+}-Doped $SrTiO_3$ Perovskite Phosphors and Their Application. *J. Mater. Chem. C* **2023**, *11* (30), 10236–10246.

(10) Cao, L.; Jia, X.; Gan, W.; Ma, C. G.; Zhang, J.; Lou, B.; Wang, J. Strong Self-Trapped Exciton Emission and Highly Efficient Near-Infrared Luminescence in Sb^{3+}-Yb^{3+} Co-Doped $Cs_2AgInCl_6$ Double Perovskite. *Adv. Funct.* **2023**, *33* (13), 2212135.

(11) Li, J.; Zhang, S.; Luo, H.; Mu, Z.; Li, Z.; Du, Q.; Feng, J.; Wu, F. Efficient near Ultraviolet to near Infrared Downconversion Photoluminescence of $La_2GeO_5:Bi^{3+}$, Nd^{3+} Phosphor for Silicon-Based Solar Cells. *Opt. Mater.* **2018**, *85*, 523–530.

(12) Liu, M.; Li, Q.; Ma, Q.; Shi, J.; Wen, C.; Xing, Z.; Zhao, J.; Wang, Z.; Wang, D.; Li, P. Down-Conversion Luminescence and Temperature Sensing Characteristics of $LaSrGaO_4:Er^{3+}$. *Luminescence* **2022**, *37* (2), 238–246.

(13) Zhang, Y.; Xin, J.; Zheng, H.; Zhao, Z.; Zhang, J.; Yang, Y.; Zheng, S.; Zhao, R.; Ding, B. Yb^{3+} Doping Monoclinic Lu_2WO_6: Near-Infrared Emission and Energy-Transfer Luminescence Mechanism. *J. Phys. Chem. C* **2018**, *122* (37), 21607–21616.

(14) Karunakaran, S. K.; Lou, C.; Arumugam, G. M.; Huihui, C.; Pribat, D. Efficiency Improvement of Si Solar Cells by Down-Shifting Ce^{3+}-Doped and down-Conversion Ce^{3+}-Yb^{3+} Co-Doped YAG Phosphors. *Sol. Energy* **2019**, *188*, 45–50.

(15) He, S.; Zhang, L.; Wu, H.; Wu, H.; Pan, G.; Hao, Z.; Zhang, X.; Zhang, L.; Zhang, H.; Zhang, J. Efficient Super Broadband NIR $Ca_2LuZr_2Al_3O_{12}:Cr^{3+},Yb^{3+}$ Garnet Phosphor for Pc-LED Light Source toward NIR Spectroscopy Applications. *Adv. Opt. Mater.* **2020**, *8* (6), 1901684.

(16) Li, J.; Chen, L.; Hao, Z.; Zhang, X.; Zhang, L.; Luo, Y.; Zhang, J. Efficient Near-Infrared Downconversion and Energy Transfer Mechanism of Ce^{3+}/Yb^{3+} Codoped Calcium Scandate Phosphor. *Inorg. Chem.* **2015**, *54* (10), 4806–4810.

(17) Zhou, R.; Wei, X.; Chen, Y.; Duan, C.; Yin, M. Ultraviolet to Near-Infrared Downconversion in Yb^{3+}-Doped Sr_2CeO_4. *Phys. Status Solidi B* **2012**, *249* (4), 818–823.

(18) Erickson, C. S.; Crane, M. J.; Milstein, T. J.; Gamelin, D. R. Photoluminescence Saturation in Quantum-Cutting Yb^{3+}-Doped $CsPb(Cl_{1-x}Br_x)_3$ Perovskite Nanocrystals: Implications for Solar Downconversion. *J. Phys. Chem. C* **2019**, *123* (19), 12474–12484.

(19) Hasegawa, T.; Kim, S. W.; Abe, Y.; Muto, M.; Watanabe, M.; Kaneko, T.; Uematsu, K.; Ishigaki, T.; Toda, K.; Sato, M.; et al. Determination of the Crystal Structure and

Photoluminescence Properties of $NaEu_{1-x}Gd_x(MoO_4)_2$ Phosphor Synthesized by a Water-Assisted Low-Temperature Synthesis Technique. *RSC Adv.* **2017**, *7* (40), 25089–25094.

(20) Posokhova, S. M.; Morozov, V. A.; Deyneko, D. V.; Nikiforov, I. V.; Redkin, B. S.; Spassky, D. A.; Belik, A. A.; Pavlova, E. T.; Posokhova, S. M. $K_5Eu_{1-x}Tb_x(MoO_4)_4$Phosphors for Solid-State Lighting Applications: Aperiodic Structures and the Tb^{3+}→Eu^{3+} Energy Transfer. *Inorg. Chem.* **2022**, *61* (20), 7910-7921.

(21) Li, K.; Van Deun, R. Color Tuning from Greenish-Yellow to Orange-Red in Thermal-Stable $KBaY(MoO_4)_3$:Dy^{3+}, Eu^{3+} Phosphors via Energy Transfer for UV W-LEDs. *ACS Appl. Electron. Mater.* **2020**, *2* (6), 1735–1744.

(22) Park, J. Y.; Chung, J. W.; Yang, H. K. Versatile Fluorescent Gd_2MoO_6:Eu^{3+} Nanophosphor for Latent Fingerprints and Anti-Counterfeiting Applications. *Ceram. Int.* **2019**, *45* (9), 11591–11599.

(23) Kneissl, M.; Seong, T.-Y.; Han, J.; Amano, H. The Emergence and Prospects of Deep-Ultraviolet Light-Emitting Diode Technologies. *Nat. Photonics* **2019**, *13* (4), 233-244.

(24) Cavalli, E.; Angiuli, F.; Belletti, A.; Boutinaud, P. Luminescence Spectroscopy of YVO_4:Ln^{3+}, Bi^{3+} (Ln^{3+} = Eu^{3+}, Sm^{3+}, Dy^{3+}) Phosphors. *Opt. Mater.* **2014**, *36* (10), 1642–1648.

(25) Xue, J.; Yu, Z.; Noh, H. M.; Lee, B. R.; Choi, B. C.; Park, S. H.; Jeong, J. H.; Du, P.; Song, M. Designing Multi-Mode Optical Thermometers via the Thermochromic $LaNbO_4$:Bi^{3+}/Ln^{3+} (Ln = Eu, Tb, Dy, Sm) Phosphors. *Chem. Eng. J.* **2021**, *415*, 128977.

(26) Güdel, H. U.; Srivastava, A. M.; Brik, M. G.; Beers, W. W.; Cohen, W. E. (INVITED) Reduced Low Temperature Lifetimes of Bi3+ Luminescence in Magnetically Ordered Host Lattices. *Opt. Mater.:X* **2021**, *12*, 100094.

(27) Arfin, H.; Kshirsagar, A. S.; Kaur, J.; Mondal, B.; Xia, Z.; Chakraborty, S.; Nag, A. Ns2Electron (Bi^{3+} and Sb^{3+}) Doping in Lead-Free Metal Halide Perovskite Derivatives. *Chem. Mater.* **2020**, *32* (24), 10255–10267.

(28) Liu, X.; Xiong, P.; Liu, H.; Wu, S.; Liu, Q.; Fu, Y.; Ma, Z.; Peng, M.; Zhang, Q. Origin of D-Band Emission in a Novel Bi^{3+}-Doped Phosphor $La_3SnGa_5O_{14}$:Bi^{3+}. *J. Mater. Chem. C* **2021**, *9* (10), 3455–3461.

(29) Huang, M. N.; Ma, Y. Y.; Huang, X. Y.; Ye, S.; Zhang, Q. Y. The Luminescence Properties of Bi^{3+} Sensitized Gd_2MoO_6:RE^{3+} (RE = Eu or Sm) Phosphors for Solar Spectral Conversion. *Spectrochim. Acta A Mol. Biomol.* **2013**, *115*, 767–771.

(30) Ye, S.; Ding, J.; Wu, Q. MMCT-Induced High-Bright Yellow Light-Emitting Phosphor Bi^{3+}-Activated Ba_2YGaO_5 Used for WLED. *Chem. Eng. J.* **2022**, *428*, 131238.

(31) Zhang, H.; Zhang, J.; Su, Y.; Zhang, X. Metal To Metal Charge Transfer Induced Efficient Yellow/Far-Red Luminescence in $Na_2Ca_3(Nb, Ta)_2O_9$:Bi^{3+} toward the Applications of White-LEDs and Plant Growth Light. *Adv. Opt. Mater.* **2022**, *10* (10), 2200150.

(32) Cao, R.; Quan, G.; Shi, Z.; Luo, Z.; Hu, Q.; Guo, S. A Double Perovskite Ca_2MgWO_6:Bi^{3+} Yellow-Emitting Phosphor: Synthesis and Luminescence Properties. *J. Lumin.* **2017**, *181*,

332–336.

(33) Back, M.; Ueda, J.; Xu, J.; Asami, K.; Amidani, L.; Trave, E.; Tanabe, S. Uncovering the Origin of the Emitting States in Bi^{3+}-Activated $CaMO_3$ (M = Zr, Sn, Ti) Perovskites: Metal-To-Metal Charge Transfer Versus s-p Transitions. *J. Phys. Chem. C* **2019**, *123* (23), 14677–14688.

(34) Colmont, M.; Boutinaud, P.; Latouche, C.; Massuyeau, F.; Huvé, M.; Zadoya, A.; Jobic, S. Origin of Luminescence in La_2MoO_6 and $La_2Mo_2O_9$ and Their Bi-Doped Variants. *Inorg. Chem.* **2020**, *59* (5), 3215–3220.

(35) Izumi, F.; Momma, K. Three-Dimensional Visualization in Powder Diffraction. *Solid State Phenom.* **2007**, *130*, 15–20.

(36) Ravel, B.; Newville, M. ATHENA, ARTEMIS, HEPHAESTUS: Data Analysis for X-Ray Absorption Spectroscopy Using IFEFFIT. *J. Synchrotron Radiat.* **2005**, *12* (4), 537–541.

(37) Giannozzi, P.; Baroni, S.; Bonini, N.; Calandra, M.; Car, R.; Cavazzoni, C.; Ceresoli, D.; Chiarotti, G. L.; Cococcioni, M.; Dabo, I.; et al. QUANTUM ESPRESSO: A Modular and Open-Source Software Project for Quantum Simulations of Materials. *J. Phys. Condens. Matter* **2009**, *21* (39), 395502.

(38) Prandini, G.; Marrazzo, A.; Castelli, I. E.; Mounet, N.; Marzari, N. Precision and Efficiency in Solid-State Pseudopotential Calculations. *NPJ Comput. Mater.* **2018**, *4* (1), 72.

(39) Anasori, B.; Shi, C.; Moon, E. J.; Xie, Y.; Voigt, C. A.; Kent, P. R. C.; May, S. J.; Billinge, S. J. L.; Barsoum, M. W.; Gogotsi, Y. Control of Electronic Properties of 2D Carbides (MXenes) by Manipulating Their Transition Metal Layers. *Nanoscale Horiz.* **2016**, *1* (3), 227–234.

(40) Obeid, M. M.; Jappor, H. R.; Al-Marzoki, K.; Al-Hydary, I. A.; Edrees, S. J.; Shukur, M. M. Unraveling the Effect of Gd Doping on the Structural, Optical, and Magnetic Properties of ZnO Based Diluted Magnetic Semiconductor Nanorods. *RSC Adv.* **2019**, *9* (57), 33207–33221.

(41) Zhao, F. A.; Xiao, H. Y.; Bai, X. M.; Liu, Z. J.; Zu, X. T. Effects of Doping Yb^{3+}, La^{3+}, Ti^{4+}, Hf^{4+}, Ce^{4+} Cations on the Mechanical Properties, Thermal Conductivity, and Electronic Structures of $Gd_2Zr_2O_7$. *J. Alloys Compd.* **2019**, *776*, 306–318.

(42) Vinoth Kumar, J.; Karthik, R.; Chen, S. M.; Natarajan, K.; Karuppiah, C.; Yang, C. C.; Muthuraj, V. 3D Flower-Like Gadolinium Molybdate Catalyst for Efficient Detection and Degradation of Organophosphate Pesticide (Fenitrothion). *ACS Appl. Mater. Interfaces* **2018**, *10* (18), 15652–15664.

(43) Krishnan, R.; Swart, H. C. Cathodoluminescence Properties of Monoclinic Phased Reddish-Orange Emitting $BaY_2(MoO_4)_4{:}Eu^{3+}$ Phosphor. *Opt. Mater.* **2020**, *99*, 109604.

(44) Li, H.; Pang, R.; Liu, G.; Sun, W.; Li, D.; Jiang, L.; Zhang, S.; Li, C.; Feng, J.; Zhang, H. Synthesis and Luminescence Properties of Bi^{3+}-Activated K_2MgGeO_4: A Promising High-Brightness Orange-Emitting Phosphor for WLEDs Conversion. *Inorg. Chem.* **2018**, *57* (19), 12303–12311.

(45) Maddi, C.; Aswin, J. R.; Scott, A.; Aslam, Z.; Willneff, E.; Adarsh, K. N. V. D.; Jha, A.

Structural, Spectroscopic, and Excitonic Dynamic Characterization in Atomically Thin Yb^{3+}-Doped MoS_2, Fabricated by Femtosecond Pulsed Laser Deposition. *Adv. Opt. Mater.* **2019**, *7* (21), 1900753.

(46) Peck, M. A.; Langell, M. A. Comparison of Nanoscaled and Bulk NiO Structural and Environmental Characteristics by XRD, XAFS, and XPS. *Chem. Mater.* **2012**, *24* (23), 4483–4490.

(47) Shannon, R. D. Revised Effective Ionic Radii and Systematic Studies of Interatomie Distances in Halides and Chaleogenides. *Acta Cryst* **1976**, *32*, 751.

(48) Momma, K.; Izumi, F. VESTA: A Three-Dimensional Visualization System for Electronic and Structural Analysis. *J Appl Crystallogr* **2008**, *41* (3), 653–658.

(49) Li, X.; Sun, Z.; Jia, M.; Liu, G.; Fu, Z.; Wei, Y.; Sheng, T.; Li, P. Investigation of the Luminescent Mechanism in Eu^{3+}-Doped Ln_2MoO_6 (Ln^{3+}= La^{3+}, Gd^{3+}, Y^{3+}) Phosphors for Warm WLED. *Mater. Res. Bull.* **2020**, *124*, 110767.

(50) Xue, J.; Li, H.; Noh, H. M.; Choi, B. C.; Park, S. H.; Jeong, J. H.; Kim, J. H. Molybdenum Substitution Induced Luminescence Enhancement in $Gd_2W_{1-x}Mo_xO_6$:Eu^{3+} Phosphors for near Ultraviolet Based Solid-State Lighting. *J. Lumin.* **2018**, *202*, 97–106.

(51) Esteban-Betegón, F.; Zaldo, C.; Cascales, C. Hydrothermal Yb^{3+}-Doped $NaGd(WO_4)_2$ Nano- and Micrometer-Sized Crystals with Preserved Photoluminescence Properties. *Chem. Mater.* **2010**, *22* (7), 2315–2324.

(52) Zhou, R.; Wei, X.; Huang, S.; Chen, Y.; Yin, M. Efficient Near-Infrared Quantum Cutting in Yb^{3+} Doped $CaNb_2O_6$ Phosphor Based on Energy Transfer. *J. Alloys Compd.* **2012**, *537*, 123–126.

(53) Wang, X.; Li, X.; Shen, R.; Xu, S.; Zhang, X.; Cheng, L.; Sun, J.; Zhang, J.; Chen, B. Optical Transition and Luminescence Properties of Sm^{3+}-Doped $YNbO_4$ Powder Phosphors. *J. Am. Ceram. Soc.* **2020**, *103* (2), 1037–1045.

(54) Kang, F.; Peng, M.; Zhang, Q.; Qiu, J. Abnormal Anti-Quenching and Controllable Multi-Transitions of Bi^{3+} Luminescence by Temperature in a Yellow-Emitting $LuVO_4$:Bi^{3+} Phosphor for UV-Converted White LEDs. *Chem. Eur. J.* **2014**, *20* (36), 11522–11530.

(55) Li, X.; Li, P.; Wang, Z.; Liu, S.; Bao, Q.; Meng, X.; Qiu, K.; Li, Y.; Li, Z.; Yang, Z. Color-Tunable Luminescence Properties of Bi^{3+} in $Ca_5(BO_3)_3F$ via Changing Site Occupation and Energy Transfer. *Chem. Mater.* **2017**, *29* (20), 8792–8803.

(56) Boutinaud, P. Revisiting the Spectroscopy of the Bi^{3+} Ion in Oxide Compounds. *Inorg. Chem.* **2013**, *52* (10), 6028–6038.

(57) Li, K.; Xue, D. Estimation of Electronegativity Values of Elements in Different Valence States. *J. Phys. Chem. A* **2006**, *110* (39), 11332–11337.

(58) Krumpel, A. H.; Boutinaud, P.; Van Der Kolk, E.; Dorenbos, P. Charge Transfer Transitions in the Transition Metal Oxides ABO_4:Ln^{3+} and APO_4:Ln^{3+} (A=La, Gd, Y, Lu, Sc; B=V, Nb, Ta; Ln=lanthanide). *J. Lumin.* **2010**, *130* (8), 1357–1365.

(59) Amer, M.; Boutinaud, P. On the Character of the Optical Transitions in Closed-Shell Transition Metal Oxides Doped with Bi^{3+}. *Phys. Chem. Chem. Phys.* **2017**, *19* (3), 2591–2596.

(60) Wang, L.; Sun, Q.; Liu, Q.; Shi, J. Investigation and Application of Quantitative Relationship between Sp Energy Levels of Bi^{3+} Ion and Host Lattice. *J. Solid State Chem.* **2012**, *191*, 142–146.

Table of Contents Graphic

Figure 1. (a) XPS survey spectra of all GMO nanophosphors. (b) Narrow scan analysis of Yb 4d (upper) and Bi 4f (bottom). (c) TEM images of all GMO nanophosphors.

Figure 2. (a) Rietveld analysis of all GMO nanophosphors: (red point) observed, (blue line) simulated, (dark-red stick) Bragg diffractions, and (green line) differences. (b) Unit cell volumes of all GMO nanophosphors. (c) Crystal structure of GMO.

Figure 3. (a) UV-vis-NIR reflectance spectra and (b) Tauc-plot of all GMO nanophosphors.

Figure 4. (a) Calculated DOS/pDOS of GMO and GMO:Bi (Substituted in Gd1 site) and (b) Enlarged ones.

Figure 5. (a) PL and PLE spectra of GMO:Yb and GMO:Bi,Yb nanophosphor in NIR region and normalized PLE spectra (inset) at 300 K. (b) PL and PLE spectra of GMO and GMO:Bi nanophosphors at 77 K in visible region. (c) PL spectra (λ_{ex}= 360 nm) and (d) decay curve (λ_{ex}= 360 nm, λ_{em}= 670 nm) of GMO:Bi,yYb (y = 0, 0.5, and 1 mol %) at 77 K.

Figure 6. Temperature-dependent PL spectra (a) in visible (GMO and GMO:Bi) and (b) NIR region (GMO:Yb and GMO:Bi,Yb). (c) Plot of the integrated emission intensity of all GMO nanophosphors.

Figure 7. (a) Time-resolved PL spectra of GMO:Bi (λ_{ex}= 355 nm) at 6 K. (b) Varied-wavelength dependent PLE spectra of GMO:Bi at 77 K (λ_{em}= 670, 570, and 530 nm).

Table 1. Fitting parameters of decay curve of GMO:Bi at 6K.

Table 2. Estimated h_e, E_{A} values and MMCT energy in each Gd site.

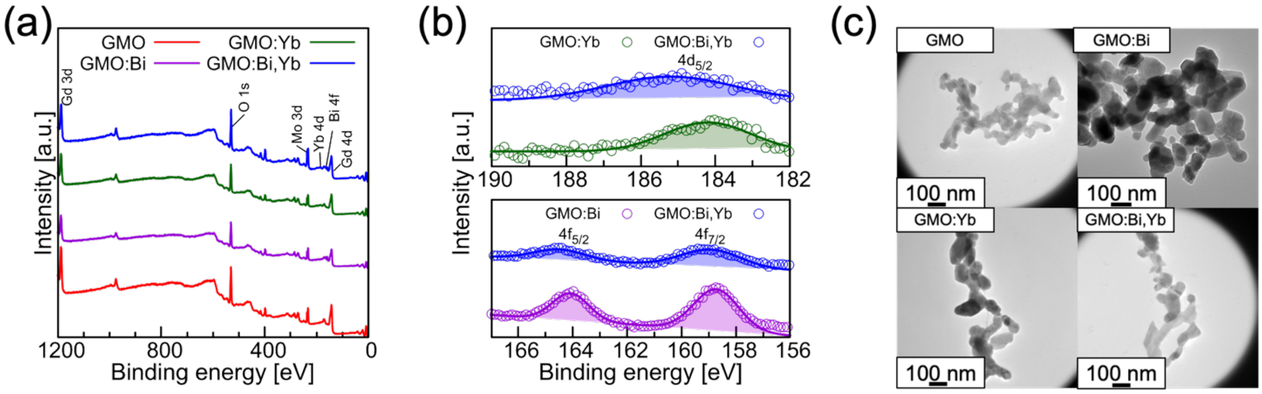

Figure 1. (a) XPS survey spectra of all GMO nanophosphors. (b) Narrow scan analysis of Yb 4d (upper) and Bi 4f (bottom). (c) TEM images of all GMO nanophosphors.

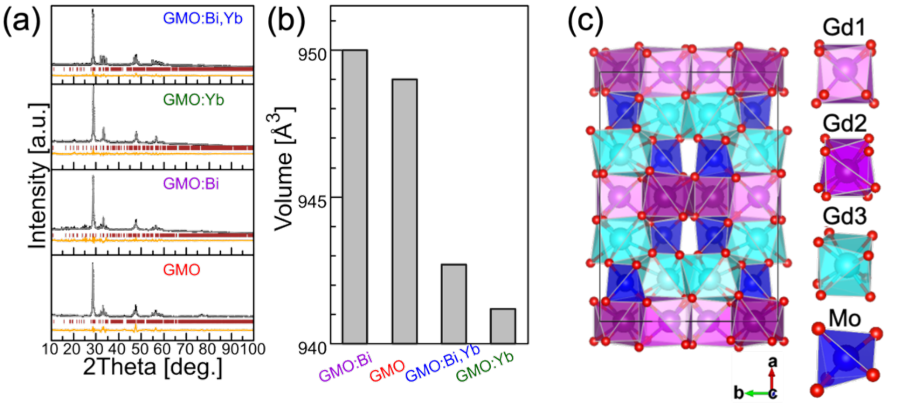

Figure 2. (a) Rietveld analysis of all GMO nanophosphors: (black point) observed, (gray line) simulated, (dark-red stick) Bragg diffractions, and (orange line) differences. (b) Unit cell volumes of all GMO nanophosphors (c) Crystal structure of GMO.

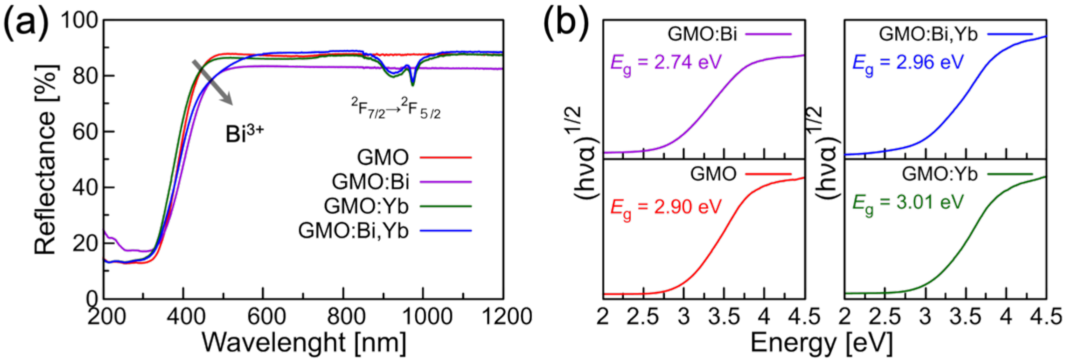

Figure 3. UV-vis-NIR reflectance spectra and (b)Tauc-plot of all GMO nanophosphors.

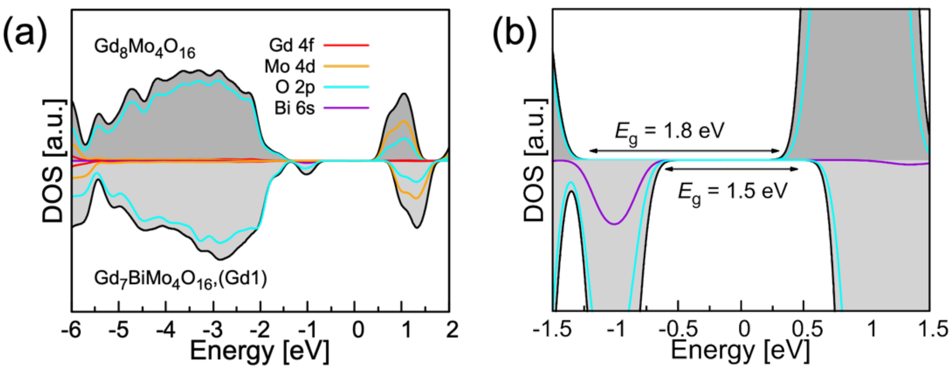

Figure 4. (a) Calculated DOS/pDOS of GMO and GMO:Bi (Substituted in Gd1 site) and (b) Enlarged ones.

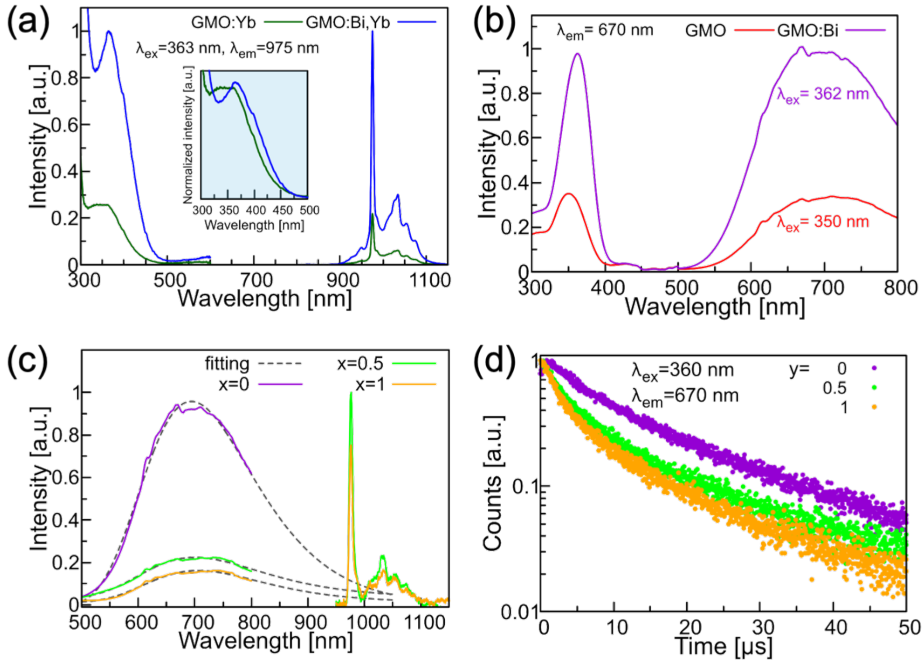

Figure 5. (a) PL and PLE spectra of GMO:Yb and GMO:Bi,Yb nanophosphor in NIR region and Normalized PLE spectra (inset) at 300 K. (b) PL and PLE spectra of GMO and GMO:Bi nanophosphors at 77 K in visible region. (c) PL spectra (λ_{ex}= 360 nm) at 77 K and (d) decay curve (λ_{ex}= 360 nm, λ_{em}= 670 nm) of GMO:Bi,yYb (y = 0, 0.5, and 1 mol %) at 77 K.

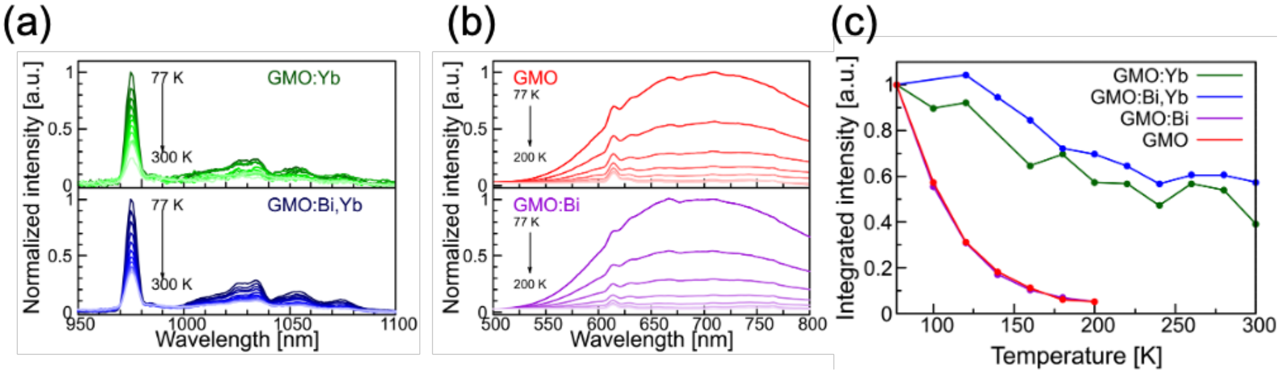

Figure 6. Temperature-dependent PL spectra in (a) visible (GMO and GMO:Bi) and NIR region (GMO:Yb and GMO:Bi,Yb). (c) Plot of the integrated emission intensity of all GMO nanophosphors.

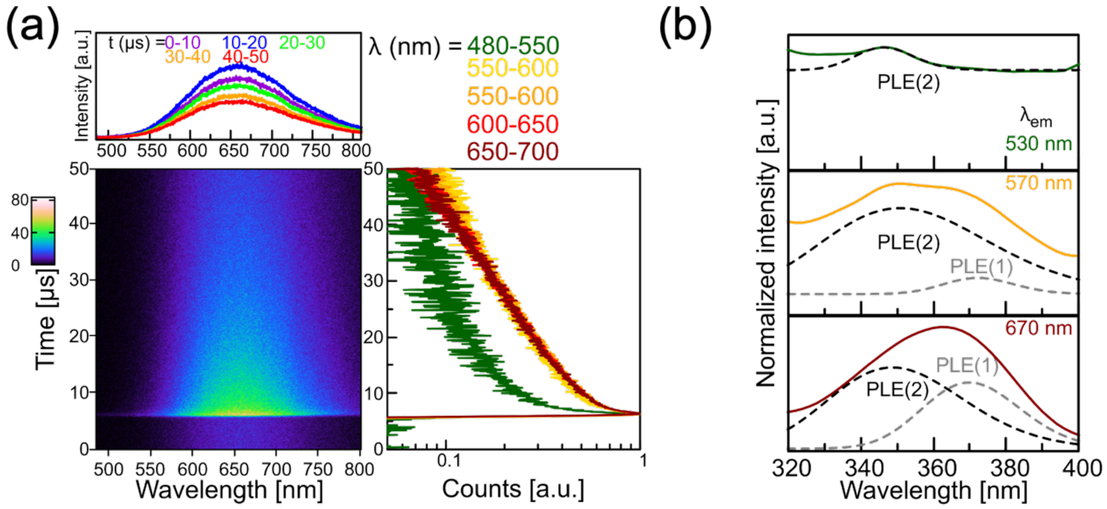

Figure 7. (a) Time-resolved PL spectra of GMO:Bi (λ_{ex}= 355 nm) at 6 K. (b) Varied-wavelength dependent PLE spectra of GMO:Bi at 77 K (λ_{em}= 670, 570, and 530 nm).

Table 1. Fitting parameters of decay curve of GMO:Bi at 6K.

	τ_1 [μs]	τ_2 [μs]
480-550 nm	9.94	0.514
550-600 nm	14.7	0.841
600-650 nm	16.3	0.833
650-700 nm	16.5	0.85
700-750 nm	16.6	1.26
750-800 nm	16.7	0.945

Table 2. Estimated h_e, E_A values and MMCT energy in each Gd site.

	Gd1	Gd2	Gd3
h_e [-]	1.57	1.59	1.61
E_A [eV]	3.33	3.44	3.30
MMCT [eV]	3.15	3.37	3.25

Graphical abstract